Aberration correction in wide-field fluorescence microscopy by segmented-pupil image interferometry

Jan Scrimgeour and Jennifer E. Curtis*

School of Physics and Parker H. Petit Institute for Bioengineering and Bioscience, Georgia Institute of Technology, Atlanta, GA 30332, USA

*Jennifer.curtis@physics.gatech.edu

Abstract: We present a new technique for the correction of optical aberrations in wide-field fluorescence microscopy. Segmented-Pupil Image Interferometry (SPII) uses a liquid crystal spatial light modulator placed in the microscope's pupil plane to split the wavefront originating from a fluorescent object into an array of individual beams. Distortion of the wavefront arising from either system or sample aberrations results in displacement of the images formed from the individual pupil segments. Analysis of image registration allows for the local tilt in the wavefront at each segment to be corrected with respect to a central reference. A second correction step optimizes the image intensity by adjusting the relative phase of each pupil segment through image interferometry. This ensures that constructive interference between all segments is achieved at the image plane. Improvements in image quality are observed when Segmented-Pupil Image Interferometry is applied to correct aberrations arising from the microscope's optical path.

OCIS codes: (180.2520) Fluorescence microscopy; (010.1080) Active or adaptive optics; (090.1970) Diffractive optics; (070.6120) Spatial light modulators; (170.0110) Imaging systems.

References and links

1. M. J. Booth, "Adaptive optics in microscopy," Philos. Transact. A Math. Phys. Eng. Sci. **365**(1861), 2829–2843 (2007).
2. J. Sebag, J. Arnaud, G. Lelièvre, J. L. Nieto, and E. L. Coarer, "High-resolution imaging using pupil segmentation," J. Opt. Soc. Am. A **7**(7), 1237–1242 (1990).
3. G. Lelievre, J.-L. Nieto, E. Thouvenot, D. Salmon, and A. Llebaria, "Very high resolution imaging using sub-pupil apertures, recentering and selection of short exposures," Astron. Astrophys. **200**, 301–311 (1988).
4. J. Liang, B. Grimm, S. Goelz, and J. F. Bille, "Objective measurement of wave aberrations of the human eye with the use of a Hartmann-Shack wave-front sensor," J. Opt. Soc. Am. A **11**(7), 1949–1957 (1994).
5. P. Prieto, E. Fernández, S. Manzanera, and P. Artal, "Adaptive optics with a programmable phase modulator: applications in the human eye," Opt. Express **12**(17), 4059–4071 (2004).
6. E. Fernandez and P. Artal, "Membrane deformable mirror for adaptive optics: performance limits in visual optics," Opt. Express **11**(9), 1056–1069 (2003).
7. J. W. Hardy, *Adaptive Optics for Astronomical Telescopes* (Oxford University Press, New York, 1988).
8. J. M. Girkin, S. Poland, and A. J. Wright, "Adaptive optics for deeper imaging of biological samples," Curr. Opin. Biotechnol. **20**(1), 106–110 (2009).
9. W. Supatto, T. V. Truong, D. Débarre, and E. Beaurepaire, "Advances in multiphoton microscopy for imaging embryos," Curr. Opin. Genet. Dev. **21**(5), 538–548 (2011).
10. P. Godara, A. M. Dubis, A. Roorda, J. L. Duncan, and J. Carroll, "Adaptive optics retinal imaging: emerging clinical applications," Optom. Vis. Sci. **87**(12), 930–941 (2010).
11. I. M. Vellekoop and A. P. Mosk, "Focusing coherent light through opaque strongly scattering media," Opt. Lett. **32**(16), 2309–2311 (2007).
12. N. Ji, D. E. Milkie, and E. Betzig, "Adaptive optics via pupil segmentation for high-resolution imaging in biological tissues," Nat. Methods **7**(2), 141–147 (2010).
13. T. Cizmar, M. Mazilu, and K. Dholakia, "In situ wavefront correction and its application to micromanipulation," Nat. Photonics **4**(6), 388–394 (2010).

#165852 - $15.00 USD Received 30 Mar 2012; revised 21 May 2012; accepted 26 May 2012; published 14 Jun 2012

14. R. W. Bowman, A. J. Wright, and M. J. Padgett, "An SLM-based Shack-Hartmann wavefront sensor for aberration correction in optical tweezers," J. Opt. **12**(12), 124004 (2010).
15. G. Hall, G. C. Spalding, P. J. Campagnola, J. G. White, and K. W. Eliceiri, "Fast localized wavefront correction using area-mapped phase-shift interferometry," Opt. Lett. **36**(15), 2892–2894 (2011).
16. D. Oron, E. Tal, and Y. Silberberg, "Scanningless depth-resolved microscopy," Opt. Express **13**(5), 1468–1476 (2005).
17. P. J. Keller, A. D. Schmidt, J. Wittbrodt, and E. H. K. Stelzer, "Reconstruction of zebrafish early embryonic development by scanned light sheet microscopy," Science **322**(5904), 1065–1069 (2008).
18. E. Fuchs, J. Jaffe, R. Long, and F. Azam, "Thin laser light sheet microscope for microbial oceanography," Opt. Express **10**(2), 145–154 (2002).

1. Introduction

Optical aberrations are often a major hurdle in the visualization of biological structures, particularly *in vivo* or in complex tissues [1]. As light passes through an organism, or part thereof, variability in the orientation of tissue surfaces and the optical properties of individual tissues encountered distort the propagating wavefront. In fluorescence microscopy these distortions make it impossible to produce a "perfect", i.e. diffraction limited, image of the specimen. Many of the techniques for countering aberrations were initially developed for astronomical telescopes but have increasingly been applied to optical microscopy as biological applications have pushed towards *in vivo* imaging. One of the earliest techniques for countering aberrations, arising from atmospheric turbulence in astronomical telescopes, is built on the realization that the effects of local wavefront tilt can be countered by dividing up the telescope's pupil into separate segments and capturing separate short exposure images from each segment simultaneously [2,3]. Selected images are then combined computationally after correcting for registration errors in the image set that are caused by local differences in the tilt of the wavefront incident at the pupil. The result is an image with enhanced resolution and contrast when compared to traditional long exposure images captured using the whole pupil.

Today, adaptive optics techniques built around the combination of wavefront detection [4] with adaptive optic devices such as spatial light modulators (SLMs) [5] or deformable mirrors [6] are enabling aberration correction in a wide variety of applications from astronomy [7] and microscopy [8,9] to medical imaging [10]. Recently, segmented-pupil techniques, in particular, have been reincarnated as a means of *in situ* aberration correction. These new methods, based on segmentation of the pupil plane using adaptive optical elements, allow for not only the correction of local wavefront tilt across the segmented pupil, but also optimization of the various paths between individual segments and the focal plane to ensure that the light from all segments interferes constructively. To date this approach has typically been used to optimize the point-spread function of focused laser beams in inhomogeneous media [11], and has found applications in two-photon microscopy [12] and optical manipulation [13,14]. An analogue of these approaches was also recently demonstrated by Hall *et al.* showing that the speed of these approaches can be increased using area based analysis [15].

In this paper we introduce an approach called segmented-pupil image interferometry (SPII) that can be used for the *in situ* correction of aberrations in wide-field fluorescence microscopy. Unlike laser-based methods where the SLM is illuminated nearly uniformly with monochromatic laser light, SPII functions with very low light levels, with a non-uniform intensity distribution in the pupil plane, and with the SLM illuminated by a distribution of wavelengths. Despite these challenges we demonstrate the correction of wavefront tilt and the optimization of pupil segment phase based on the interference of fluorescence images originating from the various pupil segments. As proof of principle we demonstrate the correction of aberrations generated in the microscope's optical path, and discuss the effect of this correction on image quality when observing samples of fluorescent microspheres and the fluorescently stained cytoskeleton of bovine pulmonary artery endothelial cells.

#165852 - $15.00 USD Received 30 Mar 2012; revised 21 May 2012; accepted 26 May 2012; published 14 Jun 2012

2. Methods

The experiments presented were performed on a bespoke fluorescence microscope built around a high numerical aperture, oil immersion, microscope objective (Nikon, CFI Apo TIRF 60X N.A. 1.49), a liquid crystal spatial light modulator (Hamamatsu, X10468-04) and a high sensitivity EMCCD camera (Andor, iXON DU897). Fluorescence was excited using a 488 nm laser line (Coherent, SapphireHP), which was controlled using an acousto-optic modulator that functions as a high-speed shutter. The laser was focused into the back focal plane of the microscope objective, emerging collimated to allow epi-fluorescence operation. Fluorescence collected by the objective was separated from the exciting laser light using a dichroic mirror and emission filter (Semrock). The back focal plane of the objective was imaged onto the center of the SLM face using a 4-f relay. A square 600 by 600 pixel region of the SLM (centered in the 800 by 600 pixel face) was used during experiments and a high frequency grating function was applied to the unused regions of the SLM face. A 500 mm focal length achromat (Thorlabs) was used to form the final image on the camera, producing an overall system magnification of 150X. Control software integrating the camera, laser excitation and spatial light modulator was written in LabView (National Instruments) and MatLab (MathWorks). Image processing was performed in ImageJ (NIH).

Samples were prepared by fixing 0.5 μm yellow green polystyrene fluorescent microspheres to the surface of a #1.5 coverglass by drying slowly in air. They were then embedded in sample mounting medium (Invitrogen, Prolong Gold) and fixed to a microscope slide using clear nail polish. Samples containing bovine pulmonary artery endothelial (BPAE) cells with the actin cytoskeleton pre-stained with Alexa Fluor 488 phalloidin were purchased from Invitrogen.

3. Results and discussion

3.1 Correction of wavefront distortion

To detect the presence of local distortions in the wavefront, the SLM was placed in the microscope's pupil plane and was used to provide active segmentation of the light. This segmentation was achieved by dividing the face of the SLM into 25 individual segments arranged in a 5-by-5 array. By default the segments were kept in an "off" state. This corresponded to the display of a high-frequency grating function that deflected the light from that segment away from the optic axis so that it formed an image outside the camera's field of view. Individual segments were turned "on" by switching the pixels in the segment to display a constant phase.

It should be noted that these "on" and "off" states are the reverse of the states used in laser-based pupil segmentation techniques [12,13,15]. This choice is necessary due to the distribution of wavelengths present in the fluorescence emission spectrum, as high-frequency grating functions result in significant dispersion of the fluorescence emission in the image plane. At low grating frequencies this dispersion is minimal and the grating function acts as a beam steering element with good fidelity. However, as the diffraction efficiency of the SLM is not 100%, we might expect a background or "ghost" image to form as a result of the undiffracted light. Since the pupil plane is illuminated by an intensity distribution that is approximately Gaussian, it will be important to consider the presence of this background image when peripheral segments in the array form images. Unlike laser illumination where the beam can be expanded to overfill the SLM face in the pupil plane, cropping the pupil plane distribution will serve to reduce the numerical aperture in the image plane. As a result, image intensities from pupil segments near the edge of the distribution (or more generally by very small pupil segments) can be close to, or lower than, the intensity of the background.

Wavefront distortion was corrected with respect to a reference segment at the center of the 5-by-5 array. The central segment was chosen to act as the reference as it is the brightest segment and, one might also assume, it is the segment least likely to be affected by

#165852 - $15.00 USD Received 30 Mar 2012; revised 21 May 2012; accepted 26 May 2012; published 14 Jun 2012

aberrations given its location on the system's optical axis. Images were collected individually from the other segments in the array, which we will call the "probe" segments to differentiate them from the reference segment. Tilt present in the wavefront incident at the probe segment is detected as a physical shift, or registration error, in the location of the image on the camera with respect to the image captured from the reference segment. After the image acquisition, the registration error of each image with respect to the reference image was calculated using a normalized cross correlation (MatLab). A background image with all segments in the "off" state was also collected and used for background subtraction during registration analysis. Any shift detected between the images was corrected through the application of an appropriate grating function to the segment corresponding to that particular image. A second image from each updated probe segment was then collected to confirm the correction of the registration error. This process is summarized in Fig. 1, where for illustrative purposes the images from the probe and reference segments are overlaid so that their registration can be compared visually both before and after correction of the wavefront distortion.

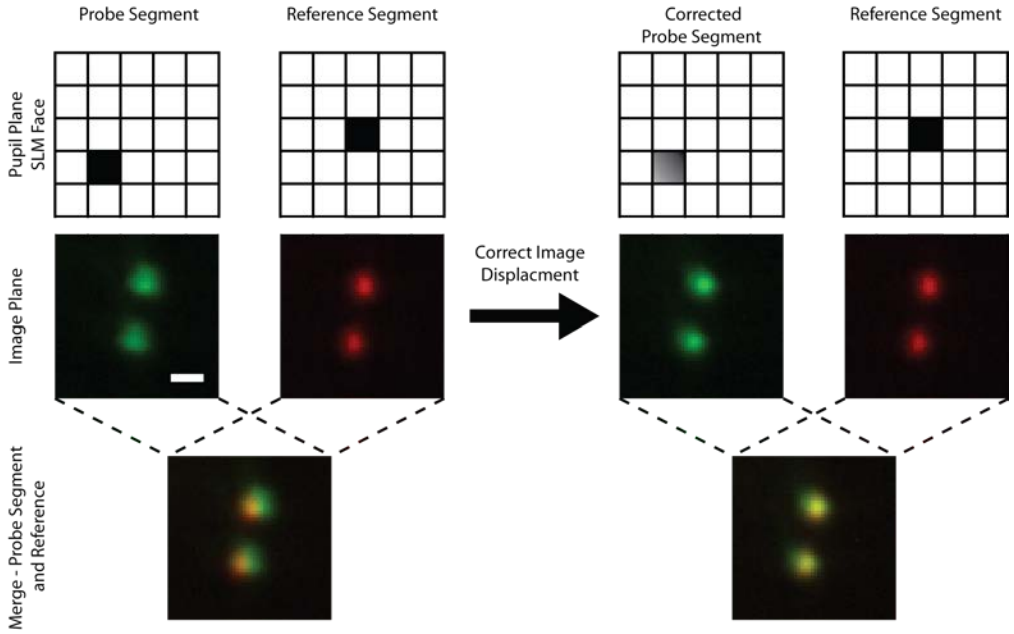

Fig. 1. Illustrates the effect of a distorted wavefront on the registration of images captured from different parts of the pupil plane (left). An appropriate grating function applied to the probe segment corrects the observed registration error (right).

3.2 Optimization of pupil segment phase

Correction of wavefront tilt is an important first step in compensating for aberrations; however it is not by itself enough to ensure the formation of an optimal image. It is equally important to establish that the light originating from the probe and reference segments undergoes constructive interference in the image plane. This can be achieved experimentally by using the SLM to apply a series of constant phase shifts to the probe segment with respect to the reference. Images collected during this series are the result of the interference between the images formed by the two active segments. The effect of interference on the captured image can be seen in Fig. 2. This shows the evolution of interference fringes in the image of a 0.5 μm fluorescent microsphere for a probe segment that directly neighbors the reference segment. The fringe spacing observed in the images is ~6 pixels. This value is in good agreement with the expected fringe spacing d of 6.3 pixels given by $d = \lambda / \theta$, calculated by

#165852 - $15.00 USD Received 30 Mar 2012; revised 21 May 2012; accepted 26 May 2012; published 14 Jun 2012

considering the interference of two plane waves, where λ is the wavelength of incident light and θ is the small angle subtended by the segments at the image plane.

Again, there are some differences here with the approaches that use direct analysis of laser interference to optimize the constructive interference between the pupil segments. These differences arise because of the limited intensity of the fluorescence emission and the intensity distribution produced in the pupil plane. These effects place a limit on the magnification of the imaging system and can restrict the ability to visualize the interference pattern. This is particularly true for the outermost probe segments where the larger separation from the reference decreases the fringe spacing. Further, the large intensity difference between the images from each segment significantly reduces the fringe visibility. As a result, we must turn to full image analysis for phase optimization rather than a point or area analysis of the interference.

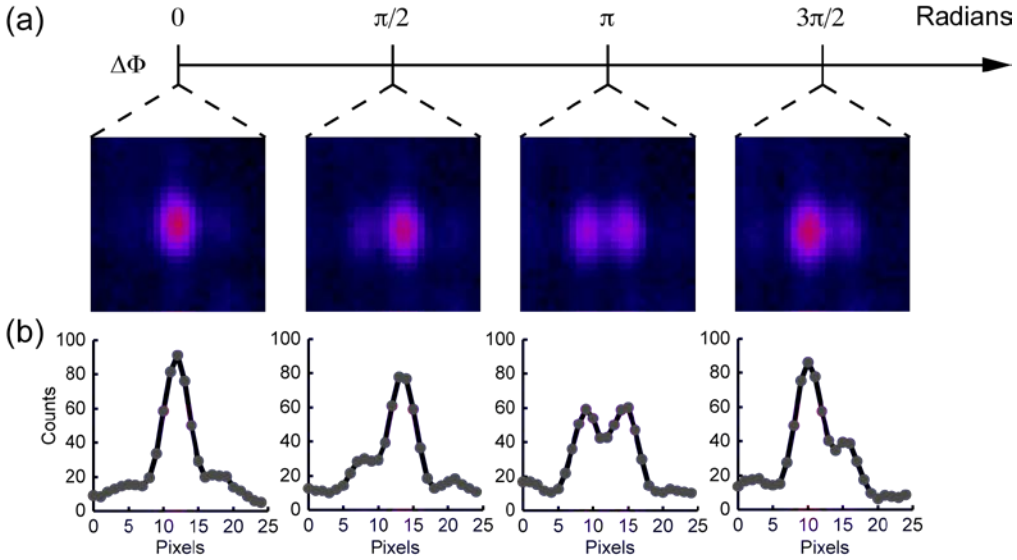

Fig. 2. Evolution of interference fringes in the image of a 0.5 μm fluorescent microsphere (a) as the phase difference (ΔΦ) between the reference segment and a neighboring probe segment is shifted between 0 and 2π radians. (b) Intensity profiles passing horizontally through the center of the fluorescent microsphere's image.

Figure 3 compares three metrics that can be used to determine the optimal phase shift to be applied to the grating function in a given probe segment. The first metric, illustrated in Fig. 3(a) is similar to that used in the optimization of focused lasers, where the intensity measured at the centroid of a single fluorescent microsphere is plotted as a function of the applied phase shift. The centroid position, determined using a particle-tracking algorithm, was determined from the original reference used in the correction of the wavefront tilt. This shows the expected cosine variation, displayed as a fit to the data, in the observed intensity versus phase shift. The second metric, shown in Fig. 3(b), tracks the mean value of the top ten percent of pixels in the image's intensity histogram. Again, this exhibits the expected cosine variation with respect to phase that was observed with metric 1. Metric 3 compares the normalized cross correlation of the acquired phase series images against the original reference image. The peak value of the cross correlation is plotted against the applied phase shift, and fit to a cosine in Fig. 3(c). While not necessarily intuitive, this metric gives an indication of how much the images in the phase series "look" like the reference. At the optimal phase shift there is minimal disruption of the image by the interference fringes, producing a larger peak in the cross correlation.

#165852 - $15.00 USD Received 30 Mar 2012; revised 21 May 2012; accepted 26 May 2012; published 14 Jun 2012

Overall, good agreement is observed in the optimal phase extracted under each of the three metrics. However, metrics 2 and 3 are ultimately more useful. While the first metric works well for images of individual microspheres, it would be challenging to implement due to its sensitivity to even small (on the order of a single pixel) shifts in the calculated centroid. In addition, this single pixel measurement requires the presence of a discrete fluorescent tracer, to function as a guide for correction. This approach is very susceptible to noise especially when considering the interference between the reference and the low intensity segments near the edge of the pupil. In contrast, metrics 2 and 3 do not require any *a priori* knowledge of the imaged object's geometry and do not require that any specific feature be identified in the image prior to determination of the optimum phase. The corrections discussed in this paper were produced using the third metric as it proved to be more reliable when considering segments with large intensity differences. By performing wavefront tilt correction and phase optimization sequentially across the whole pupil, a kinoform correcting the measured aberrations is generated.

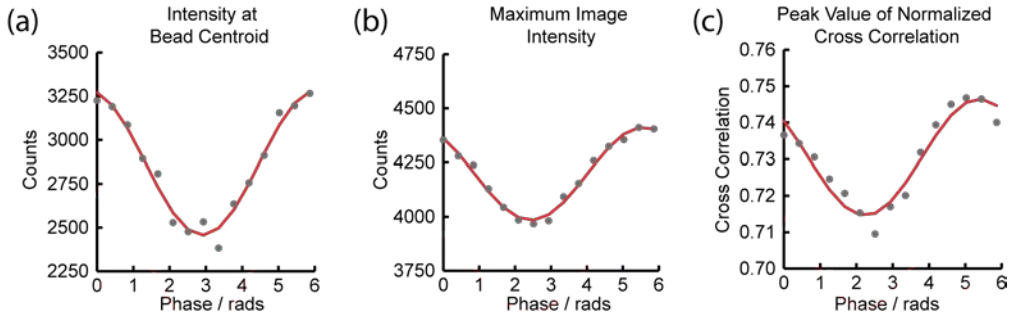

Fig. 3. Comparison of methods for optimizing the path difference between a probe segment and the reference. (a) Direct tracking of the intensity at the centroid of a microsphere, (b) Tracking the average value in the top 10% of pixel intensities, and (c) tracking the peak value of the cross correlation between the captured images and the original reference image. In each case the data is displayed with the fitted curve used to extract the optimal phase adjustment for the corrected pupil segment.

3.3 Aberration correction

A kinoform that contains the 5-by-5 array of pupil segments with corrections calculated by the SPII method for our microscope's light path is shown in Fig. 4(a). It is notable that the intensity falling on the corner segments is so low that the image analysis does not provide a meaningful correction for these segments. The full correction was generated in about 2 minutes, only 20 seconds of which was used to capture the 400 images required. The remaining time was in part due to a conservative estimate of the update time for the SLM, which accounted for 40 seconds. However, it was mainly due to the overheads associated with image processing in MatLab and with the method used to trigger the capture of images from the camera. In the future, tighter hardware integration and the use of a lower level programming language would likely reduce this time substantially.

To demonstrate the effect of the SPII correction on image quality we compare fluorescence images captured using no aberration correction with those captured after the application of the SPII correction. The results of this comparison are shown in Figs. 4(b) and 4(c). Figure 4(b) compares the images of 0.5 μm fluorescent microspheres taken using no aberration correction, then the SPII correction and finally the SLM's factory correction. The curvature of the SLM's polished silicon backplane is the major source of aberrations in the microscope's optical path. As a result we will consider the factory correction be the ideal correction for the aberrations in the system and use it as a convenient benchmark to assess the SPII method. Images of clustered fluorescent microspheres captured in the plane of "best focus" for each case, show that the SPII approach significantly improves the ability to resolve

#165852 - $15.00 USD Received 30 Mar 2012; revised 21 May 2012; accepted 26 May 2012; published 14 Jun 2012

the individual microspheres within the cluster. Through-focus image series reveal significant astigmatism present in the case of no applied correction, as evidenced by the asymmetry of the image seen in the planes neighboring the plane of best focus. With the SPII correction applied, most of this asymmetry is removed and a shift in the plane of best focus of ~200 nm is observed. Qualitatively, the results obtained with the SPII correction offer a marked improvement in image quality over the uncorrected system, and the image quality appears to compare well with that observed when the factory correction is applied to the SLM.

Figure 4(c) compares of the intensity profile of a representative fluorescent microsphere imaged under each of the three correction conditions studied. This further confirms that the SPII correction compares well with the factory correction. After comparing the images of several microspheres the SPII correction returns the microsphere's intensity to 89 ± 3% of the intensity observed when using the spatial light modulator's factory correction. The intensity of the microspheres with no applied correction was 78 ± 2% of that observed when the factory correction was applied. The observed full widths at half maximum (FWHM) of line profiles taken through images of microspheres under each correction were 5.8 ± 0.2, 4.4 ± 0.1 and 4.1 ± 0.1 pixels for no correction, the SPII correction and the factory correction respectively. The SPII correction improves the typical microsphere FWHM to 107% for the value obtained with the factory correction. This is compared to 141% of the benchmark set by the factory correction, when no correction was applied.

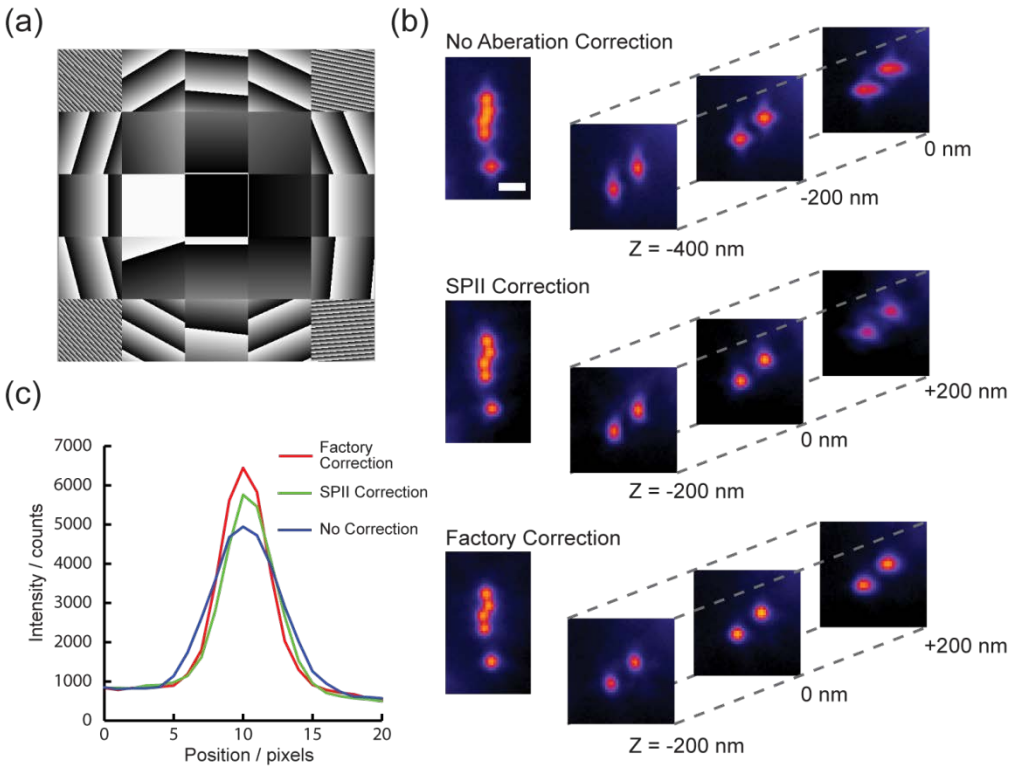

Fig. 4. Correction of system aberrations. (a) Shows the kinoform produced by the SPII correction procedure. (b) Shows the result of imaging of 0.5 μm fluorescent microspheres using no aberration correction, SPII correction, and the SLM's factory correction respectively. For each condition an image of a cluster of microspheres is shown alongside a through-focus image series. Scale bar 1 μm. (c) Shows a comparison between the intensity profiles of a single 0.5 μm fluorescent microsphere captured using no correction (blue line), the SPII correction (green line) and the SLM factory correction (red line). There are 105 nm per pixel.

#165852 - $15.00 USD Received 30 Mar 2012; revised 21 May 2012; accepted 26 May 2012; published 14 Jun 2012

Figure 5 further demonstrates the improvement in image quality that results from application of the SPII correction, this time when imaging the fluorescently stained actin network in BPAE cells. White arrows indicate features of the actin cytoskeleton where the improved contrast is evident after the application of the SPII correction. This improvement in image contrast is a function of the improvement in the microscope's resolution, as demonstrated in Fig. 4, and a reduction in the background signal (pink arrows Fig. 5) when aberration correction is used.

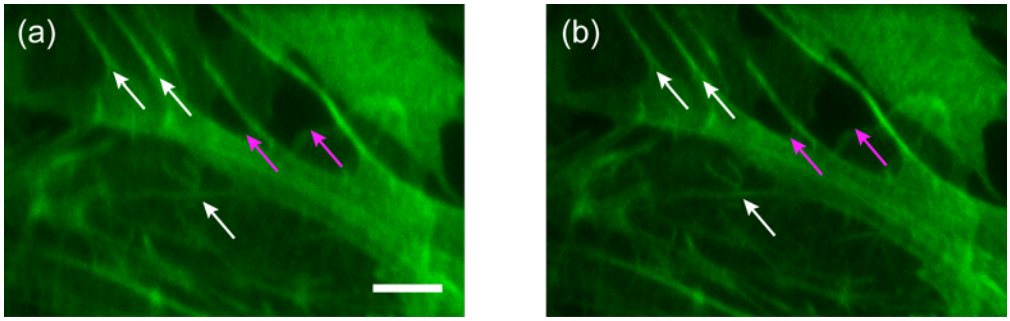

Fig. 5. Illustrates the improvements in visualization of the cytoskeleton in BPAE cells resulting from the application of the SPII correction. (a) no applied correction, (b) SPII correction. Arrows indicate features of interest. Scale bar 5 μm.

4. Conclusions

In summary, we have demonstrated that SPII is a technique capable of *in situ* correction of optical aberrations in wide-field fluorescence microscopy. Here, we have demonstrated the correction of system aberrations using a 5-by-5 segmentation of the pupil plane as proof of principle that segmented pupil techniques can be applied in a wide-field geometry. In this example, the majority of the aberrations present in the optical system arise from the SLM itself. Evaluation of the SPII correction against an optimized correction, supplied by the SLM manufacturer, showed that it performed well but did not provide full correction of the aberrations present. Future implementations of SPII could be enhanced by the incorporation of more segments in the correction allowing it to correct aberrations that contain higher frequency variations in the wavefront. However, the uniform square grid geometry quickly fails as a means of expanding this technique as the intensity falling on the peripheral segments falls below the threshold for successful image analysis. This might be addressed by using an adaptive grid where segment sizes are weighted to account for the non-uniform intensity distribution in the pupil plane. This would provide a compromise between the desire to use as many segments as possible in the correction and the need to maintain workable intensity levels at the outermost segments in the array. While the discussion of SPII method was limited to aberrations present in the microscope's optical path, this approach can be applied to the more general case where aberrations arise from other sources, such heterogeneous biological tissues. The application of the segmented-pupil interferometry methodology to wide-field fluorescence microscopy shows the robustness of this class of techniques for the *in situ* correction of local aberrations. This technique may also find applications in conjunction with non-scanning microscopy techniques such as temporally focused [16] or light sheet illumination [17,18].

Acknowledgments

This work was funded by the Human Frontiers in Science Program (RGP0013/2010).

#165852 - $15.00 USD Received 30 Mar 2012; revised 21 May 2012; accepted 26 May 2012; published 14 Jun 2012